

## Article

# Study on the Pre-Oxidation and Resulting Oxidation Mechanism and Kinetics of Mo-9Si-8B Alloy

Cheng Wang<sup>1,\*</sup>, Qiuliang Li<sup>1</sup> , Zhenping Guo<sup>1</sup>, Xiangrong Li<sup>1</sup>, Xiangyu Ding<sup>1,2</sup>, Xin Li<sup>1</sup>, Zhuoyue Li<sup>1</sup> and Bin Li<sup>1</sup>

<sup>1</sup> Fundamentals Department, Air Force Engineering University, Xi'an 710038, China; qiuliang\_95@163.com (Q.L.); pluto\_70@126.com (Z.G.); lixiangrong0925@126.com (X.L.); dingxiangyu@nchu.edu.cn (X.D.); lx202006t10@163.com (X.L.); lz\_980512@163.com (Z.L.); 15770518701@163.com (B.L.)

<sup>2</sup> School of Aircraft Engineering, Nanchang Hangkong University, Nanchang 330063, China

\* Correspondence: warrant\_74@126.com; Tel.: +86-1363-028-5102

**Abstract:** Molybdenum silicon boron alloy is regarded as the next generation of superalloy that is expected to replace nickel-based superalloys. However, the high-temperature oxidation resistance of Mo-Si-B alloy has always been an issue worth studying. In this study, Mo-9Si-8B alloy was prepared via a plasma oscillatory pressure sintering process and pre-oxidized at 1300 °C while maintaining a certain balance of mechanical and oxidation properties. The influence of the oxide protective layer on its performance at high temperature of 1150 °C was explored, the micro-mechanism of its performance and its failure mode of the hinge-locking mechanism was illustrated, and finally, its oxidation kinetics was inferred. In conclusion, pre-oxidized Mo-9Si-8B (at.%) alloy did play a role in delaying the oxidation process during the initial period of cyclic oxidation. However, with the increase of cyclic oxidation time, the improvement of high-temperature oxidation resistance was limited.

**Keywords:** pre-oxidation; molybdenum silicon boron alloy; hinge locking



**Citation:** Wang, C.; Li, Q.; Guo, Z.; Li, X.; Ding, X.; Li, X.; Li, Z.; Li, B. Study on the Pre-Oxidation and Resulting Oxidation Mechanism and Kinetics of Mo-9Si-8B Alloy. *Materials* **2021**, *14*, 5309. <https://doi.org/10.3390/ma14185309>

Academic Editor: Filippo Berto

Received: 16 July 2021

Accepted: 23 August 2021

Published: 15 September 2021

**Publisher's Note:** MDPI stays neutral with regard to jurisdictional claims in published maps and institutional affiliations.



**Copyright:** © 2021 by the authors. Licensee MDPI, Basel, Switzerland. This article is an open access article distributed under the terms and conditions of the Creative Commons Attribution (CC BY) license (<https://creativecommons.org/licenses/by/4.0/>).

## 1. Introduction

For existing nickel-based superalloys, they could be used at around 900 °C without the coating and cooling system. Even with the addition of the coating and cooling system, the nickel-based alloy could only work at about 1150 °C [1], which had reached its maximum limit and resulted in a huge reduction in the efficiency of the turbine engine. The use of non-cooled engine components will greatly reduce the amount of cooling air and increase thrust. The calculations in Figure 1a show that for every 1% reduction in nozzle guide vane (NGV) cooling gas, the engine thrust increases by 0.84%, the engine fuel flow increases by 1.43%, and the specific fuel consumption (SFC) increases by 0.54%. Mo-Si, Nb-Si, and Si-C ceramic matrix composites were the main candidates for high-temperature parts of aero-engines in the future [2]. The specific strength of the Si-C ceramic matrix composites was low, and its intrinsic brittleness was too large. It was not suitable for load-bearing parts of complex shapes in high-temperature circumstances, and it was difficult to connect ceramic matrix composites with metal materials [3]. The specific strength and oxidation resistance of Nb-Si alloy above 1300 °C were obviously weaker than that of Mo-Si alloy [1–4]. It had been difficult to meet the high-temperature resistance requirements of high-temperature parts [5]. Mo-Si-B alloy as one of the Mo-Si alloys was the attractive material considered as the key direction of the future development of superalloys, which had been explored for decades. Due to its remarkable properties, it had been expected to be an alternative for next-generation turbine engine blades. The Mo-Si-B alloy exhibited outstanding mechanical properties, high-temperature oxidation resistance, good creep resistance, and high melting point. However, it is hard for the Mo-Si-B alloy to keep both the mechanical properties and

high-temperature oxidation resistance excellent. While maintaining certain mechanical properties, it is still a problem to continue to maintain and improve the oxidation resistance. There were several methods of approaching this problem: (1) The first method was through microalloying, doping with trace elements to form stable oxides, reducing the diffusion rate of oxygen to the internal matrix, and improving the adhesion of the oxide layer. Pogozhev found that adding a small amount of Hf can enhance the wettability of the oxide layer [6], and it played a role in changing the microstructure of the oxide film, improving the toughness of the oxide film, and preventing the oxide film from cracking [7]. (2) The second way was to design a suitable Si/B ratio. Supatarawanich et al. [8] had found that Mo-Si-B alloys had better oxidation resistance at 1300 °C with the Si/B ratio close to 1. (3) The third way was to improve the oxidation resistance of the alloy by refining the grain, but as the grain boundaries increase, Si was more likely to segregate to the grain boundary, causing the strength of the grain boundary to decrease [9]. (4) At last, the pre-oxidation method was also reckoned as one of the potential ways to solve this problem.

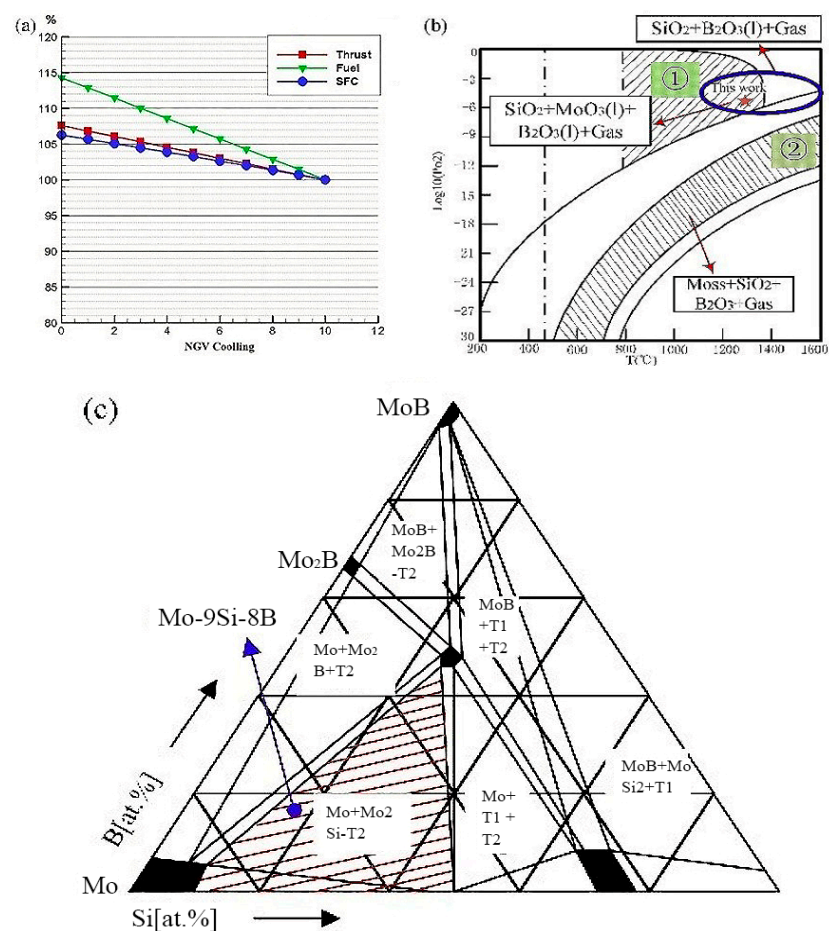


**Figure 1.** (a) Effect of high-conductivity cooling air volume on engine performance in our calculation: Thrust is getting higher with the decrease of the cooling air volume. (b) Calculated oxygen partial pressure diagram for the Mo-9Si-8B-O system Adapted from [10]. (c) Isothermal section of Mo-Si-B at 1600 °C, the composition chosen for this study was marked Adapted from [11].

## 2. Materials and Methods

The samples were prepared from elemental powder mixtures of Mo, Si, and B of 99.95 wt.%, 99.99 wt.%, 99.95 wt.% purity with an average particle size of 2.0–3.5 μm, 3.0–5.0 μm, and 0.5–1.0 μm, respectively. The alloy composition chosen for this study was located within the three phases field between α-Mo + Mo<sub>5</sub>SiB<sub>2</sub> + MoSi<sub>3</sub> (Figure 1c). All samples were processed by a powder metallurgical (PM) route. The mixed powders were put into the planetary mill (QM-3SP04, Nanjing Laibu Technology Industrial Co., LTD,

Nanjing, China) with a speed of 300 rpm and a powder-to-ball weight ratio of 1:10. The ball mill rotated forward and reversed for 12 h respectively to get a uniform mixture. At the same time, it also included a plasma oscillation sintering process, which adopted 6 h heat preservation time and a regular pressure oscillation curve, keeping the frequency at 9 Hz (periodic change). In addition, the oscillatory sintering furnace independently designed by Morningstar Weike Co., Ltd. (Ningbo, China) can greatly increase the density of the alloy.

The pre-oxidation behavior of the Mo-9Si-8B alloy was investigated. The pre-oxidation specimens were prepared by cutting cylindrical samples with dimensions of  $\Phi 20 \times 5$  mm. Then, the cylindrical samples were grounded with SiC paper to a grit of 2000 and polished with 1 and 0.25  $\mu\text{m}$  diamond paste. Next, the samples were pre-oxidized at 1300 °C under  $10^{-6}$  Pa oxygen partial pressure for 2 h (Figure 1b). At last, the cyclic oxidation experiment was implemented. The cyclic oxidation experiment was to keep the temperature at 1150 °C for 50 h to verify the effectiveness of the pre-oxidation. Samples used for the oxidation test were taken out to weigh at 0.5 h, 1 h, 5 h, 10 h, 20 h, 30 h, and 50 h, respectively, and cooled to room temperature in air at the time of each weight.

The microstructure was etched using the Murakami's etch (an aqueous solution of 10 vol.% potassium ferricyanide and 10 vol.% sodium hydroxide) before using the scanning electron microscope (SEM, TESCAN, Brno, Czech Republic). Meanwhile, element diffusion and distribution were explored by energy dispersion spectroscopy (EDS, Oxford Instruments Co., Oxford, UK). After the oxidation, the constituent phases and structure of the oxidation scale were identified by X-ray diffraction using the Cu-K $\alpha$  radiation (XRD, XRD7000S, Shimadzu, Tokyo, Japan).

### 3. Results and Discussion

#### 3.1. Microstructures of the Plasma Oscillation Sintered Composites

Figure 2a showed the surface microstructure of the sintered alloy, and the high magnification was revealed in Figure 2b. The continuous Mo<sub>ss</sub> (light phase, Mo solid solution), Mo<sub>5</sub>SiB<sub>2</sub> (dark phase), and Mo<sub>3</sub>Si (gray phase) were confirmed by the XRD result, and the distribution of these phases was inferred by EDS scanning. The intermetallic phase can be seen clearly and dispersed in the Mo<sub>ss</sub> base phase. The area ratio was used to replace the volume fraction, and the average volume fraction of Mo<sub>ss</sub> phase was 54.9 vol.% calculated 10 times by Image-Pro Plus software (6.0). To some extent, the volume fraction of the Mo<sub>ss</sub> phase was close to the expected target of 50 vol.%, which committed to maintaining relatively balanced mechanical properties and antioxidant properties [12–14]. The density increase of oscillatory sintering can be measured by the Archimedes suspension wire method. Compared with traditional hot-pressing sintering, this density was increased by 9.25 g/cm<sup>3</sup>, and its relative density reached 97.78%.

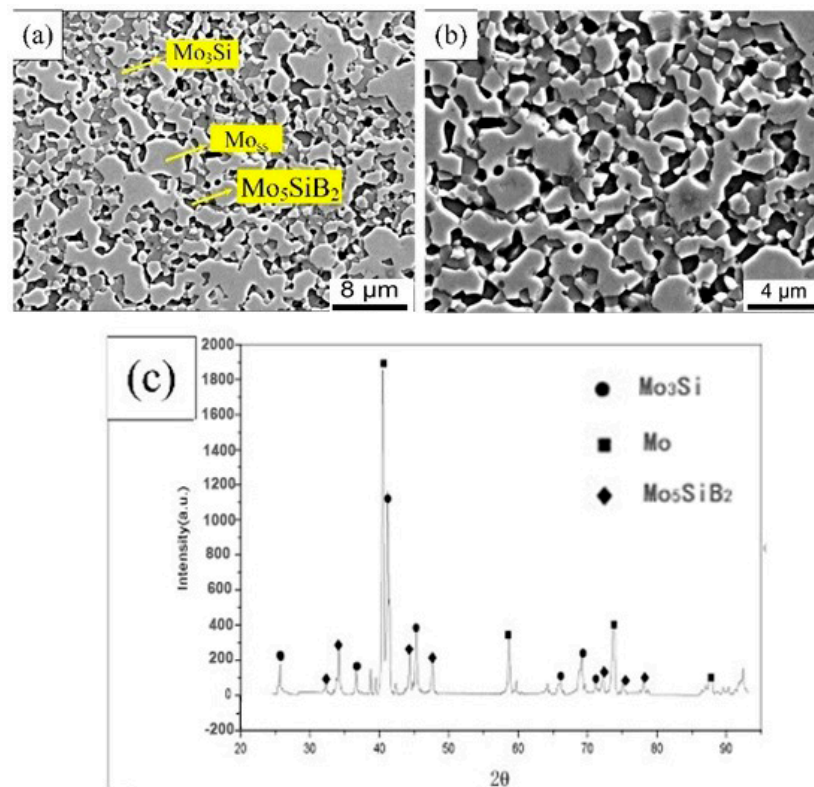


**Figure 2.** Microstructure of alloy prepared by plasma concussion sintering: (a) 3000×; (b) 5000×; (c) X-ray diffraction pattern.

### 3.2. Cross-Section of Pre-Oxidation Alloy

As shown in Figure 3a,c, after 30 min of pre-oxidation, a discontinuous oxide layer was formed on the outermost surface of the alloy (Figure 3a,c). Under the outermost oxide layer, an intermediate layer of 30.6 μm existed on the substrate (Figure 3c). After investigation and analysis by EDS, the black granular part was SiO<sub>2</sub> oxide, and the rest was almost the Mo<sub>ss</sub> phase. The region 'A' is the region that firstly underwent an oxidation reaction to form a large amount of silica, which can be confirmed by the EDS scanning results marked 'A' in Figure 3b. The formation of silicon dioxide consumed the intermetallic phase, causing the unoxidized part of the outermost layer to belong to the Mo<sub>ss</sub> phase, which was consistent with Mendiratta's results [15]. Another point worth noting was that in the first oxidized area 'A', the reduction of the distribution of boron can be clearly found, which indicated that the boron oxide volatilized rapidly at this temperature, leading to the loss of B element. Figure 3d,e showed the morphology of the surface oxide layer after 1 h. It could be seen that a ≈1–2 μm thin containing-SiO<sub>2</sub> layer had been formed. The most important point was that in the contact part between the outermost oxide and the intermediate layer, there were black silicon dioxide particles grown from the substrate to link the oxide layer with the intermediate layer, which acted as a mechanical locking [16]. It closely connected the SiO<sub>2</sub> oxide layer with the substrate, which reinforced the protection. After 2 h of pre-oxidation as observed in Figure 3f, the depth of mechanical locking was further deepened, and a dense silica protective layer was formed on the surface of the substrate, which adhered well to the substrate.

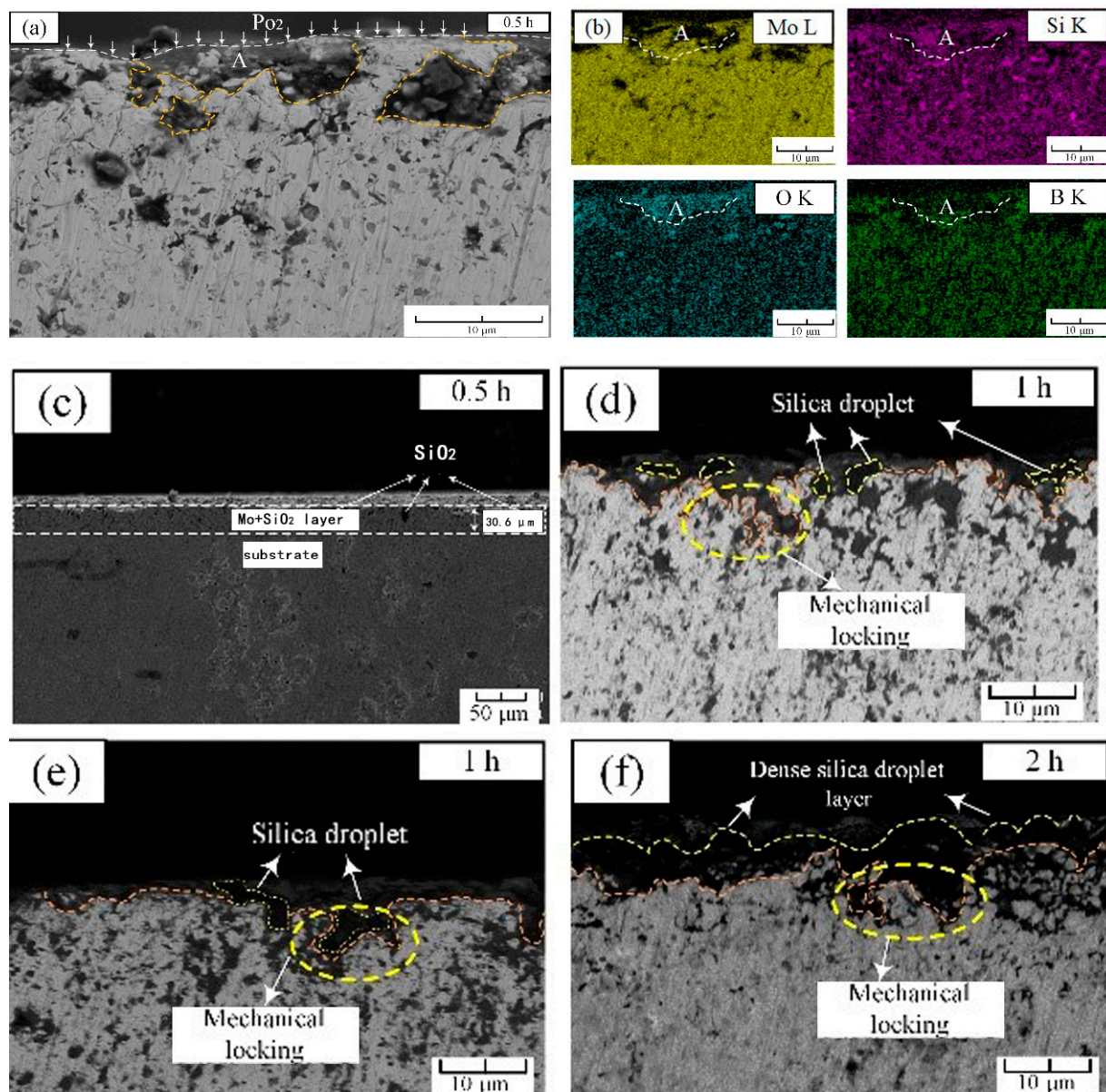


**Figure 3.** Cross-sectional morphology of pre-oxidized alloy at 1300 °C: (a) pre-oxidation for 0.5 h; (b) local EDS mappings in (a); (c) macro-image of (a) for 30 min; (d,e) pre-oxidation for 1 h; (f) pre-oxidation for 2 h.

### 3.3. EDS Analysis and Surface Morphology of the Pre-Oxidized Alloy

Figure 4 showed the surface morphology of the sample after 2 h of pre-oxidation, as observed in the secondary electron and backscatter modes, respectively. It can be seen from Figure 4a that a dense layer with no bubbles completely covered the surface of the substrate. We have selected five spots to do EDS, and all these spots have similar results. A typical result of these spots is shown in Figure 4b. From the analysis of the EDS results, it can be concluded that there may exist a certain amount of boron oxide and silicon dioxide under this condition. In addition, under this condition, almost no Mo content appeared on the surface, which implied that there was almost no molybdenum oxidation on the surface. After 2 h of pre-oxidation, the surface of the sample formed a dense borosilicate layer.

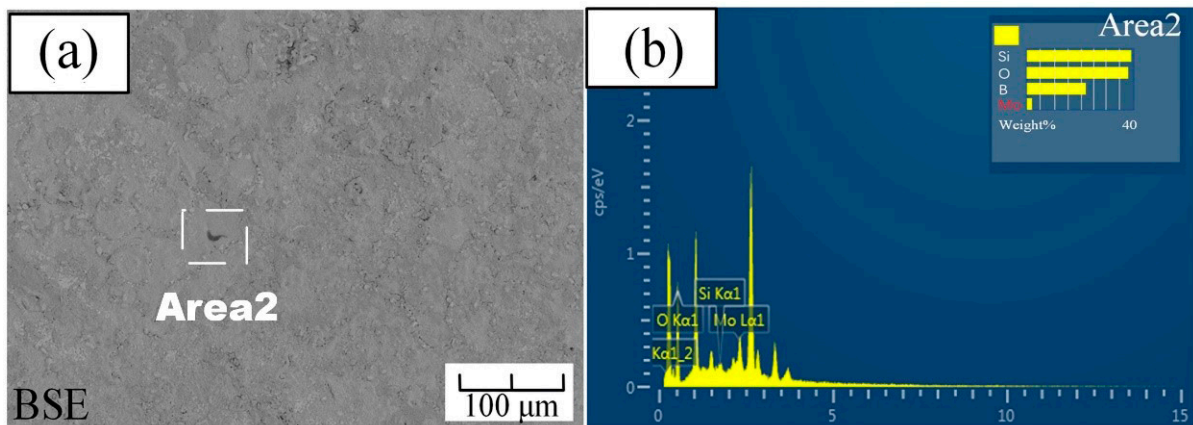


**Figure 4.** Pre-oxidized surface of the Mo-9Si-8B alloy for 2 h: (a) backscattered electron image; (b) EDS of Area 2 in (a).

### 3.4. Oxidation Behavior of Mo-Si-B Alloy at 1150 °C

In this study, the protective effect of the pre-oxidation layer at 1150 °C was discussed here. The engine starting process was similar to the cyclic oxidation, so the cyclic oxidation at 1150 °C was selected. The surface and cross-sectional morphology of cyclic oxidation at 1150 °C after 50 h of oxidation is shown in Figure 5. Figure 5a showed the appearance of holes, cracks, and protrusions on the surface. At the same time, Figure 5b contained a large number of cracks and there even existed oxide-scale spalling. The existence of the pores may be due to the volatilization of molybdenum oxide inside, which caused the bubbles to rush out of the external oxide layer and remain holes. In an air atmosphere, the higher oxygen concentration can no longer maintain the selective oxidation conditions of silicide and borides. Due to a large amount of Mo element, oxygen reached the oxide/matrix interface and reacted with Mo atoms to form MoO<sub>3</sub> and MoO<sub>2</sub>. The formation of MoO<sub>3</sub> was quickly lost in the form of gas, resulting in the rupture of the borosilicate protective layer on the surface, further accelerating the process of oxygen invasion. The cyclic oxidation process had undergone multiple heating/cooling processes, which can be explained according to Pilling's classical "PBR" theory (Pilling \ Bedworth Ratio) [17]. In the process of metal forming oxide, the volume changes to produce growth strain, which is defined as "PBR":

$$PBR = \frac{V_{OX}}{V_M} \quad (1)$$

where  $V_{ox}$  is the volume of oxide formed, and  $V_M$  is the volume of metal consumed.

The oxide film expanded horizontally and vertically, and it was divided into horizontal growth and vertical growth. Since the thermal expansion coefficient of the oxide layer and the substrate were different, the degree of volume expansion was inconsistent, which will cause internal stress. When  $PBR > 1$ , compressive stress was generated in the oxide film; when  $PBR < 1$ , tensile stress was generated in the oxide film [18]. In this study, the  $PBR$  of Mo<sub>3</sub>Si to SiO<sub>2</sub> of the pre-oxidized alloy is about 2.1, and the  $PBR$  of Mo<sub>5</sub>SiB<sub>2</sub> to SiO<sub>2</sub> and B<sub>2</sub>O<sub>3</sub> is about 1.01 based on the oxide layer formed by the pre-oxidation and the volume of metal consumed, which can refer to Li's calculation method [18]. As a result, the pre-oxidized film generated compressive stress, and the subsequent cyclic oxidation further led to inconsistent expansion and contraction rates. The oxide layer shrunk and expanded less than the substrate. Therefore, the cooling process of the oxide layer was bound by the substrate. When the internal stress was greater than the critical stress that the oxide layer can withstand, the stress will cause cracks and spalling behavior. Furthermore, as shown in Figure 3, the mechanical locking mechanism played a very good 'hinge-locking' function at first, which held the borosilicate layer tightly on the surface of the substrate, but as the internal oxide changed from molybdenum-based to molybdenum oxide in Figure 4d and Figure 5e, we suspected it was its coefficient of thermal expansion changing from  $6 \times 10^{-6} \text{ K}^{-1}$  to  $5 \times 10^{-6} \text{ K}^{-1}$  that resulted in the reduction of the transverse pressure

on the  $\text{SiO}_2$  embedded in the substrate. As the  $\text{MoO}_3$  rushed out in the form of bubbles, a loose  $\text{MoO}_3$  area was formed, which further released the lateral pressure on  $\text{SiO}_2$  and gradually led to the failure of the mechanical locking mechanism.

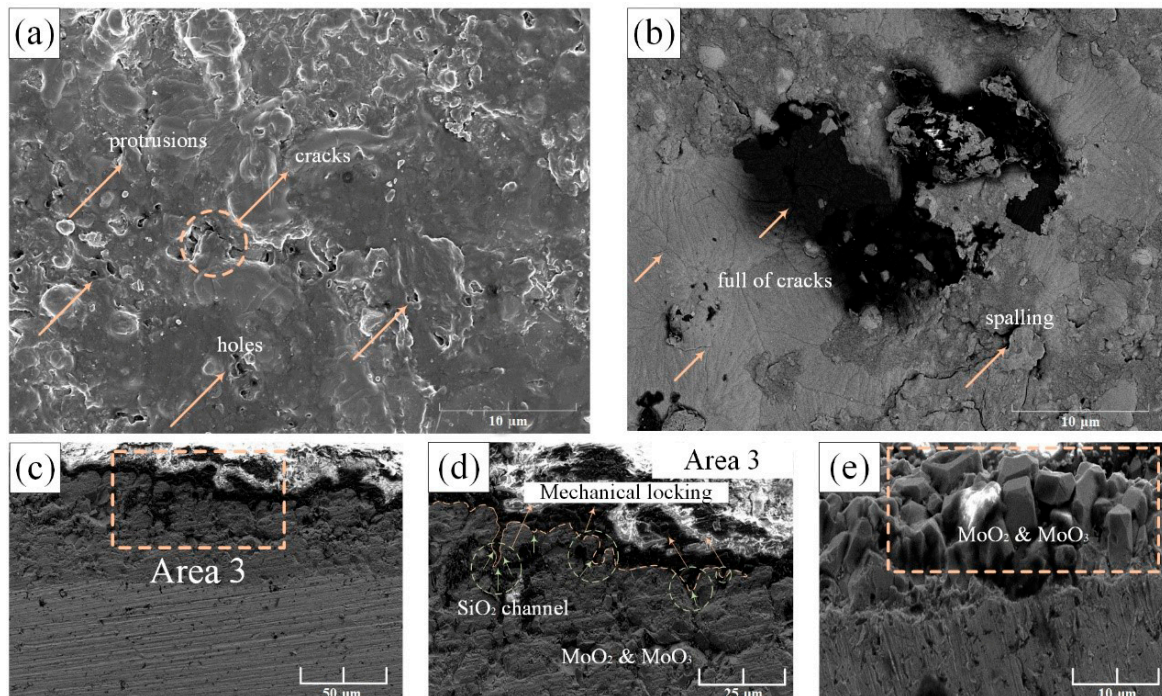


**Figure 5.** SEM microstructures of pre-oxidized Mo-9Si-8B composite after oxidation in air at 1150 °C for 50 h: (a,b) are surface SEM images of the alloy; (c) cross-sectional morphology of the edge; (d) local magnification of area 3 in (a); (e) molybdenum oxide products grown from the substrate.

As shown in Figure 6a, the oxidation mass loss curve at 1150 °C was plotted. The pre-oxidized sample had a mass loss of  $-107.5 \text{ mg/cm}^2$  after 50 h of exposure to the air, which was  $-198.3 \text{ mg/cm}^2$  compared to the sample without pre-oxidation treatment. Although the weightlessness has been reduced by nearly  $91 \text{ mg/cm}^2$ , the weightlessness of 50 h had not been substantially improved. However, it can be seen from the partially enlarged view of Figure 6b that the pre-oxidation layer played a very good protective role in the initial period and delayed the progress of the oxidation behavior.

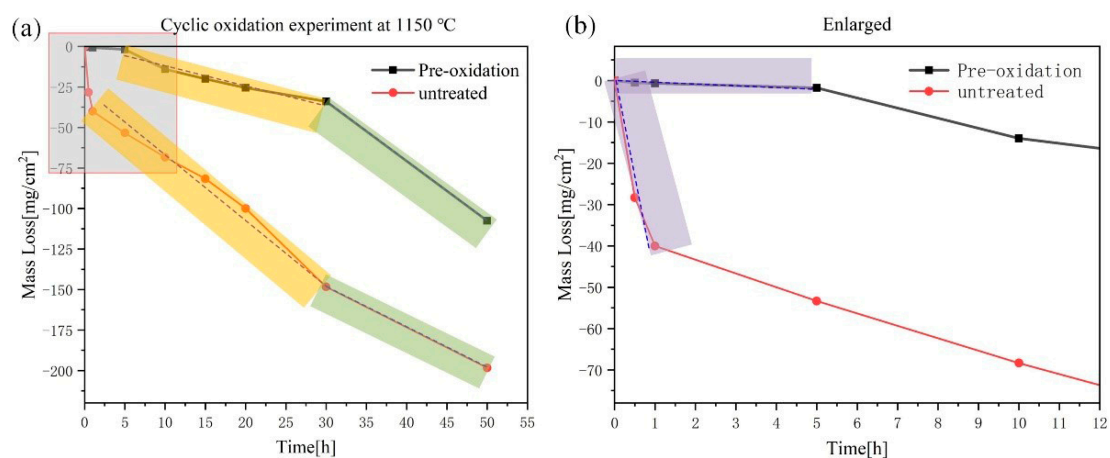


**Figure 6.** Oxidation kinetic curve at 1150 °C for 50 h in air: (a) oxidation mass loss curves of pre-oxidized and untreated samples; (b) local enlarged part in (a).

According to the mass loss trend, the curve was divided into three parts (Figure 6). At the initial stage, the mass loss of the pre-oxidation samples was significantly lower than that of the untreated samples, which indicated that the dense oxide layer effectively reduced the rate of oxygen diffusion. In the subsequent stage, the mass loss of the pre-oxidized samples increased significantly, indicating that under the condition of high oxygen partial pressure, the thinner protective layer formed by the pre-oxidation could not completely prevent the intrusion of oxygen. The mass loss rate of MoO<sub>3</sub> was faster than the formation of the borosilicate layer, showing linear weight loss. When the oxidation time exceeded 30 h, the pre-oxidation samples had a severe mass loss. However, the alloy experienced a mass loss with  $-14 \text{ mg/cm}^2$  during the first 10 h, which was relatively better than Rioult's data of  $-17 \text{ mg/cm}^2$  mass loss in 10 h at 1100 °C [19,20]. It was worth pointing out that in the first 5 h earlier, the alloy experienced a mass loss of  $-1.8 \text{ mg/cm}^2$ , which was better than Helmick's data of  $-40 \text{ mg/cm}^2$  [21]. Hence, it exhibited an improved oxidation resistance in the initial stage at 1150 °C.

### 3.5. Inferred Analysis and Mechanisms

The formation of the oxide layer includes two parts: the diffusion process and the chemical reaction. The diffusion process requires a chemical potential gradient as a driving force. In the chemical reaction process, the chemical reaction proceeds in the direction of the decrease of Gibbs free enthalpy. The pre-oxidation process is carried out at 1300 °C, so the Gibbs free energy of each phase reacting with 1 mol of oxygen is calculated. The calculation of Gibbs free energy usually includes two calculation methods: one uses the standard reaction heat effect calculation, and the other uses the standard reaction difference entropy calculation. In this study, a simplified algorithm is used: the material Gibbs free energy function method [22,23]. The algorithm is based on the classic algorithm without any assumptions, and the result is exactly the same as the classic algorithm.

$$\Delta G_T^0 = \Delta H_{T_0}^0 - T\Delta\phi'_T \quad (2)$$

where  $\Delta H_{T_0}^0$  is the standard enthalpy of reaction at  $T_0$ ,  $\Delta\phi'_T$  is the Gibbs free energy function of the reaction,  $\Delta G_T^0$  represents the Gibbs free energy of the reaction.

First, the Gibbs free energy function of the reaction at 1300 °C (1573 K) ( $\Delta\phi'_{1573}$ ) is calculated by the following linear Equation (4). All the results are shown in Table 1.

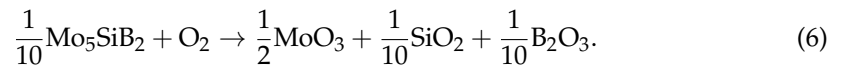
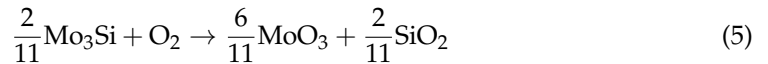
$$\Delta\phi'_{1573} = \Delta\phi'_{1500} + \frac{\Delta\phi'_{1600} - \Delta\phi'_{1500}}{1600 - 1500}(1573 - 1500) \quad (3)$$

**Table 1.** Thermodynamic data of some materials.

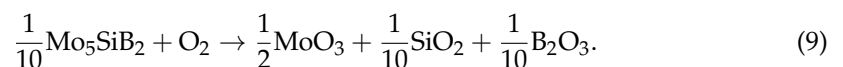
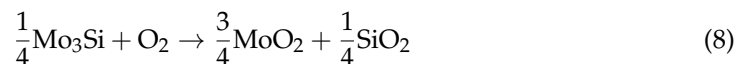
| Species                          | $\Delta H_{298}^0$ (J/mol) | $\phi'_T$ (1500 K) | $\phi'_T$ (1600 K) | $\Delta S_{298}^0$ J/(mol·K) | $\phi'_T$ (1573 K) |
|----------------------------------|----------------------------|--------------------|--------------------|------------------------------|--------------------|
| Si                               | 0                          | 37.991             | 39.325             | 18.828                       | 38.965             |
| SiO <sub>2</sub>                 | -847,260                   | 94.535             | 98.027             | 46.861                       | 97.084             |
| B <sub>2</sub> O <sub>3</sub>    | -1,252,188                 | 160.427            | 166.642            | 78.404                       | 164.964            |
| Mo                               | 0                          | 50.011             | 51.467             | 28.606                       | 51.074             |
| O <sub>2</sub>                   | 0                          | 230.835            | 232.579            | 205.016                      | 232.108            |
| Mo <sub>3</sub> Si               | -116,399                   | 187.129            | 192.698            | 106.148                      | 191.194            |
| Mo <sub>5</sub> SiB <sub>2</sub> | -309,616                   | 369.280            | 380.389            | 207.342                      | 377.389            |
| MoO <sub>2</sub>                 | -587,852                   | 106.092            | 110.217            | 49.999                       | 109.103            |
| MoO <sub>3</sub>                 | -360,661                   | 338.169            | 342.156            | 279.910                      | 341.079            |

Second, under 1300 °C and different oxygen partial pressure, the following three kinds of reaction equations may exist:

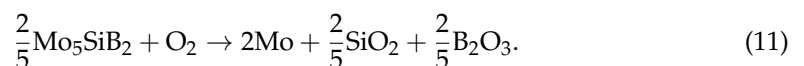
In the case of high oxygen partial pressure:



In the case of further reduction of oxygen partial pressure:



In the case of low oxygen partial pressure:



Third, the diffusion path and the oxidation products of each equation are determined by the oxygen partial pressure at the oxide/matrix interface. The oxygen partial pressure of each equation is calculated according to the following Equation (12):

$$\log P_{\text{O}_2} = \Delta G_T^0 / 2.303RT \quad (12)$$

where  $R$  is the gas constant, and  $P_{\text{O}_2}$  represents the equilibrium oxygen partial pressure.

According to the above data and equations, the Gibbs free energy and oxygen partial pressure of each phase of Mo-Si-B alloy reacting with 1 mol oxygen is calculated as follows.

It can be seen from Table 2 that the Gibbs free energy of Equation (6) and Equation (7) is less than that of Equation (5), and similarly, the Gibbs free energy of Equation (9) and Equation (10) is also less than that of Equation (8). It is all pointed that the oxidation behavior of the intermetallic phase is before the  $\text{Mo}_{\text{ss}}$  phase at three levels of oxygen partial pressure. In particular, the oxygen partial pressure required for the reaction of Equation (5) is at the level of  $1.10 \times 10^{-6}$ , which is slightly higher than the level of designed ambient oxygen partial pressure. It indicates that the activity of generating  $\text{MoO}_3$  is inhibited from the beginning and proceeds at a very slow rate; then, it evaporates instantly at a high temperature of 1300 °C. The outermost intermetallic phase is oxidized to produce  $\text{SiO}_2$  melt and  $\text{B}_2\text{O}_3$ . Although the viscosity of  $\text{SiO}_2$  decreases at high temperatures, it is still as high as  $10^9$  dpa·s. As shown in Figure 7a, in the early stage of pre-oxidation, the B source provided from the substrate is divided into two parts: one part evaporates directly from the substrate, and the other part enters the formed  $\text{SiO}_2$  melt.  $\text{B}_2\text{O}_3(\text{g})$  that existed in the  $\text{SiO}_2$  melt gradually increases from the bottom to the top due to changes in pressure. The volume change promotes the liquid up and down convection; the melt  $\text{SiO}_2$  collapses and flows after blasting. Therefore, the presence of  $\text{B}_2\text{O}_3$  increases the flow force of high-viscosity  $\text{SiO}_2$  melt and accelerates the covering process. Then, most of  $\text{B}_2\text{O}_3$  escapes from the borosilicate layer at a very fast evaporation rate, leaving a high-viscosity  $\text{SiO}_2$  layer, reducing the oxygen diffusion rate by six orders of magnitude [24]. With the increase of the depth of the matrix, the partial pressure of oxygen is further reduced, and the selective oxidation of Si occurs. The intermetallic phase is consumed to provide the Si/B source [25]. After two hours, an intermediate layer of  $\text{Mo}_{\text{ss}}$  distributed with  $\text{SiO}_2$  granular is formed.

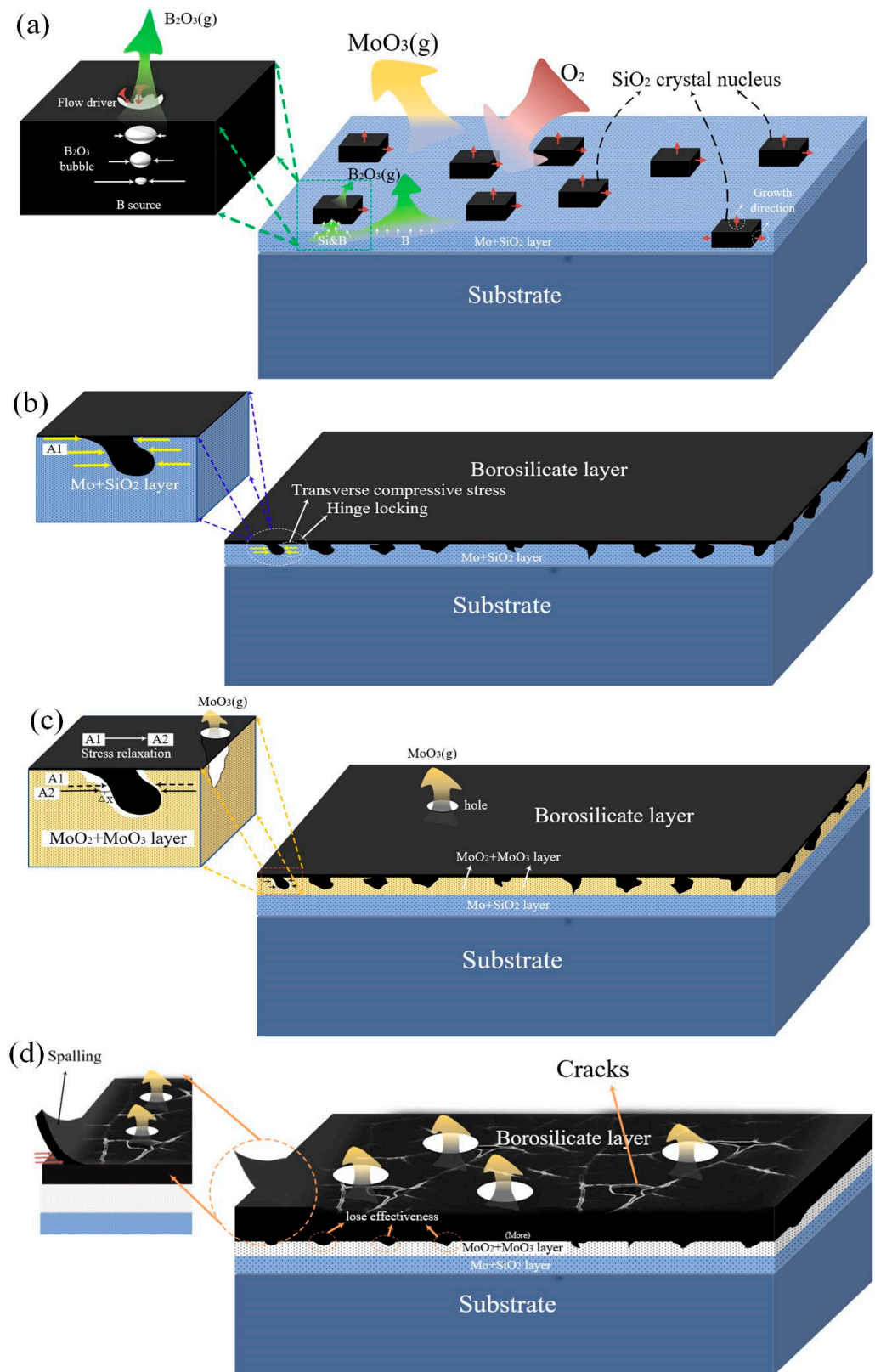


**Figure 7.** Pre-oxidation and cyclic oxidation mechanism diagram:(a,b) are pre-oxidation progress at 1300 °C; (c,d) are cyclic oxidation progress at 1150 °C.

**Table 2.** Values of  $\Delta G_T^\theta$  and  $P_{O_2}$  of the Equation (4) to Equation (11).

| Equations                   | Equation (5)           | Equation (6)           | Equation (7)           | Equation (8)           |
|-----------------------------|------------------------|------------------------|------------------------|------------------------|
| $\Delta G_T^\theta$ (J/mol) | −179,453.39            | −230,225.86            | −244,327.40            | −314,025.73            |
| $P_{O_2}$ (Pa)              | $1.10 \times 10^{-6}$  | $2.27 \times 10^{-8}$  | $7.72 \times 10^{-9}$  | $3.75 \times 10^{-11}$ |
| Equations                   | Equation (9)           | Equation (10)          | Equation (11)          | Equation (12)          |
| $\Delta G_T^\theta$ (J/mol) | −350,203.87            | −355,661.54            | −458,738.29            | −438,933.16            |
| $P_{O_2}$ (Pa)              | $2.36 \times 10^{-12}$ | $1.55 \times 10^{-12}$ | $5.77 \times 10^{-16}$ | $2.67 \times 10^{-15}$ |

As shown in Figure 7b, the B-poor borosilicate layer formed by pre-oxidation has a mechanical locking effect and plays a role of articulation. According to the calculated PRB values of  $2.1 > 1$  and  $1.01 > 1$ , the  $SiO_2$  formed by the first selective oxidation will expand along with the lateral growth and the longitudinal growth. Since the longitudinal volume expansion hardly generates stress, the inwardly extending  $SiO_2$  particles undergo lateral expansion to generate compressive stress. The pre-oxidized intermediate layer is the Mo-based layer, and the thermal expansion coefficient is 10 times larger than the  $SiO_2$  melt. The lateral volume expansion causes stronger compressive stress, forming a locking mechanism, increasing the adhesion to the substrate.

The pre-oxidized samples were cyclically oxidized at 1150 °C for 50 h. The parabolic mass loss proved to be protective for the initial period, but then, it changed to linear weight loss, and the protective layer became ineffective. One is because  $MoO_2$  and  $MoO_3$  are generated with the increase of oxygen partial pressure and the inward diffusion of oxygen.  $MoO_3$  evaporated, forming small bubbles, and it escapes the borosilicate layer, causing holes and flakes in the protective layer [26–28]. The pores make  $MoO_3$  a loose structure and become a channel for oxygen diffusion and further intrusion. Then, the internal matrix appeared as a large mass loss. On the other hand, it is caused by the inconsistent thermal expansion coefficient of the protective layer. The thermal expansion coefficient of the produced  $MoO_3$  and  $MoO_2$  ( $5 \times 10^{-6} K^{-1}$ ) intermediate layer is lower than  $Mo_{ss}$  ( $6 \times 10^{-6} K^{-1}$ ), which weakens the volumetric compressive stress of  $SiO_2$  particles with a ‘mechanical locking’ effect. The loose structure of  $MoO_3$  and  $MoO_2$  further released the compressive stress, as shown in Figure 7c, resulting in the loss of the  $SiO_2$  mechanical locking function that functions as a ‘hinge locking’. At last, the adhesion of the protective layer decreases, spalling occurs, and the protective layer fails, which confirms the results in Figure 4. At last, the mechanism diagram of the pre-oxidation of Mo-Si-B alloy and the cyclic oxidation at 1150 °C is illustrated in Figure 7, which is contributed to understand the mechanism of pre-oxidation behavior of Mo-Si-B alloy.

#### 4. Conclusions

In this paper, the pre-oxidation of the Mo-9Si-8B alloy was carried out under the conditions of 1300 °C and  $10^{-6}$  Pa oxygen partial pressure. The microstructure evolution process and the pre-oxidation mechanism were illustrated and explained, and then the cyclic oxidation was carried out at 1150 °C for 50 h. The oxidation kinetics was discussed here, and the following conclusions were drawn:

1. Pre-oxidation formed a borosilicate layer with a thickness of 3–5  $\mu m$ . The selective oxidation of Si resulted in the formation of  $SiO_2$ , and its lateral growth produced compressive stress, which led to a ‘hinge-locking’ mechanism and increased the adhesion to the substrate.
2. In the pre-oxidation stage, part of  $B_2O_3$  escaped directly from the substrate, and the other part entered the  $SiO_2$  layer. Its volume change promoted liquid flow and the movement of the bubbles from the bottom to top promoted the convection of  $SiO_2$  melt. Eventually, blasting caused  $SiO_2$  liquid to collapse and flow, which improved the fluidity of the protective layer.
3. The reason for the failure of the ‘hinge-locking’ mechanism in the cyclic oxidation stage was that the  $MoO_3$  and  $MoO_2$  intermediate layer replaced the position of the

- Mo<sub>ss</sub> phase, and the thermal expansion coefficient of MoO<sub>3</sub> and MoO<sub>2</sub> intermediate layers decreased, which led to the decrease of the pressure on the SiO<sub>2</sub> particles with the locking effect. In addition, the loose structure caused by MoO<sub>3</sub> bubbles further released the pressure stress, resulting in the failure of the ‘link-locking’ mechanism.
- Pre-oxidation played a role in delaying the oxidation process in the initial stage of the cyclic oxidation, but as the cycle oxidation time increased, its protective effect was lost and entered the rapid weight loss stage, but the 10 h oxidation result still had certain advantages.

**Author Contributions:** Conceptualization, C.W. and Z.G.; methodology, X.L. (Xiangrong Li); writing—original draft preparation, Q.L., X.L. (Xin Li), and X.D.; writing—review and editing, Q.L.; supervision, B.L. and Z.L.; All authors have read and agreed to the published version of the manuscript.

**Funding:** This research was funded by the “Shanxi Provincial Key Research and Development Project (2020GY-307)”.

**Institutional Review Board Statement:** Not applicable.

**Informed Consent Statement:** Not applicable.

**Data Availability Statement:** The data presented in this study cannot be shared at this time as the data also forms part of an ongoing study.

**Acknowledgments:** The authors were appreciated for the precious comments and suggestions of the editors and reviewers.

**Conflicts of Interest:** The authors declare no conflict of interest.

## References

- Dimiduk, D.M.; Perepezko, J.H. Mo-Si-B alloys: Developing a revolutionary turbine-engine material. *Mrs Bull.* **2003**, *28*, 639–645. [[CrossRef](#)]
- Zhao, J.C.; Westbrook, J.H. Ultrahigh-Temperature materials for jet engines. *Mrs Bull.* **2003**, *28*, 622–630. [[CrossRef](#)]
- Li, W.; Ai, T.; Dong, H.; Zhang, G. Tribological properties of Mo-Si-B alloys doped with La<sub>2</sub>O<sub>3</sub> and tested at 293–1173 K. *Materials* **2019**, *12*, 2011. [[CrossRef](#)]
- Bewlay, B.P.; Jackson, M.R.; Subramanian, P.R.; Zhao, J.-C. A review of very-high-temperature Nb-silicide-based composites. *Metall. Mater. Trans. A* **2003**, *34*, 2043–2052. [[CrossRef](#)]
- Jin, X.C.; Li, P.; Hou, C.; Wang, X.B.; Fan, X.L.; Lu, C.S.; Xiao, G.S.; Shu, X.F. Oxidation behaviors of ZrB<sub>2</sub> based ultra-high temperature ceramics under compressive stress. *Ceram. Int.* **2019**, *45*, 7278–7285. [[CrossRef](#)]
- Pogozhev, Y.S.; Lemesheva, M.V.; Potanin, A.Y. Heretophase ceramics in the Hf-Si-Mo-B system fabricated by the combination of SHS and hot pressing methods. *Russ. J. Non-Ferr. Met.* **2019**, *60*, 380–389. [[CrossRef](#)]
- Grammenos, I.; Tsakiroopoulos, P. Study of the role of Al, Cr and Ti additions in the microstructure of Nb-18Si-5Hf base alloys. *Intermetallics* **2010**, *18*, 242. [[CrossRef](#)]
- Supatarawanich, V.; Johnson, D.R.; Liu, C.T. Oxidation behavior of multiphase Mo-Si-B alloys. *Intermetallics* **2004**, *12*, 721–725. [[CrossRef](#)]
- Sturm, D. The influence of silicon on the strength and fracture toughness of molybdenum. *Mater. Sci. Eng. A* **2006**, *463*, 107–114. [[CrossRef](#)]
- Kruzic, J.J.; Schneibel, J.H.; Ritchie, R.O. Ambient-to-elevated temperature fracture and fatigue properties of Mo-Si-B alloys: Role of microstructure. *Metall. Mater. Trans. A* **2005**, *36*, 2393–2402. [[CrossRef](#)]
- Choe, H.; Schneibel, J.H.; Ritchie, R.O. On the fracture and fatigue properties of Mo-Mo<sub>3</sub>Si-Mo<sub>5</sub>SiB<sub>2</sub> refractory intermetallic alloys at ambient to elevated temperatures (25 °C to 1300 °C). *Metall. Mater. Trans. A* **2003**, *34*, 225. [[CrossRef](#)]
- Jehanno, P.; Heilmaier, M.; Saage, H.; Heyse, H.; Böning, M.; Kestler, H.; Schneibel, J.H. Superplasticity of a multiphase refractory Mo-Si-B alloy. *Scr. Mater.* **2006**, *55*, 525–528. [[CrossRef](#)]
- Burk, S.; Gorr, B.; Christ, H.-J. High temperature oxidation of Mo-Si-B alloys: Effect of low and very low oxygen partial pressures. *Acta Mater.* **2010**, *58*, 6154–6165. [[CrossRef](#)]
- Nomura, N.; Suzuki, T.; Yoshimi, K.; Hanada, S. Microstructure and oxidation resistance of a plasma sprayed Mo-Si-B multiphase alloy coating. *Intermetallics*. **2003**, *11*, 735–742. [[CrossRef](#)]
- Mendiratta, M.G.; Parthasarathy, T.A.; Dimiduk, D.M. Oxidation behavior of αMo-Mo<sub>3</sub>Si-Mo<sub>5</sub>SiB<sub>2</sub> (T2) three phase system. *Intermetallics* **2002**, *10*, 225–232. [[CrossRef](#)]
- Wen, S.H.; Zhou, C.G.; Sha, J.B. Improvement of oxidation resistance of a Mo-62Si-5B (at.%) alloy at 1250 °C and 1350 °C via an in situ pre-formed SiO<sub>2</sub> fabricated by spark plasma sintering. *Corros. Sci.* **2017**, *127*, 175–185. [[CrossRef](#)]

17. Kumar, N.K.; Das, J.; Mitra, R. Effect of moist air and minor zr addition on oxidation behavior of arc-melted multiphase Mo-Si-B alloys in the temperature range of 1000 °C–1300 °C. *Oxid. Met.* **2020**, *93*, 483–513. [[CrossRef](#)]
18. Li, M.; Qian, Y.; Xin, L. Volume ratio of an oxide to the metal. *Corros. Sci. Prot. Technol.* **1999**, *11*, 284–289.
19. Chen, Y.; Wang, C.G.; Zhao, W.; Lu, W.B.; Chen, A.T.; Tan, T.T. Fabrication of a SiC/Si/MoSi<sub>2</sub> multi-coating on graphite materials by a two-step technique. *Ceram. Int.* **2012**, *38*, 2165–2170. [[CrossRef](#)]
20. Rioult, F.A.; Imhoff, S.D.; Sakidj, R. Transient oxidation of Mo-Si-B alloys: Effect of the microstructure size scale. *Acta Mater.* **2009**, *57*, 4600–4613. [[CrossRef](#)]
21. Helmick, D.A.; Meier, G.H.; Pettit, F.S. High temperature oxidation behavior of a Mo-3Si-1B(wt.%) alloy. *Mater. High Temp.* **2005**, *22*, 293–307. [[CrossRef](#)]
22. Majumdar, S.; Gorr, B.; Christ, H.-J. Oxidation mechanisms of lanthanum-alloyed Mo-Si-B. *Corros. Sci.* **2014**, *88*, 360–371. [[CrossRef](#)]
23. Rosales, I.; Martinez, H.; Bahena, D.; Ruiz, J.A.; Guardian, R.; Colin, J. Oxidation performance of Mo<sub>3</sub>Si with Al additions. *Corros. Sci.* **2008**, *51*, 534–538. [[CrossRef](#)]
24. Li, B.; Wang, J.; Chen, X. High-temperature oxidation response of Mo-Si-B composites with TiO<sub>2</sub>W/SiCW addition. *Ceram. Int.* **2019**, *45*, 16046–16053. [[CrossRef](#)]
25. Makineni, S.K.; Kini, A.R.; Jägle, E.A.; Springer, H.; Raabe, D.; Gault, B. Synthesis and stabilization of a new phase regime in a Mo-Si-B based alloy by laser-based additive manufacturing. *Acta Mater.* **2018**, *151*, 31–40. [[CrossRef](#)]
26. Choi, W.J.; Lee, S.Y.; Park, C.W.; Park, J.H.; Byun, J.M.; Kim, Y.D. Effect of titanium addition on mechanical properties of Mo-Si-B alloys. *Int. J. Refract. Met. Hard Mater.* **2019**, *80*, 238–242. [[CrossRef](#)]
27. Byun, J.M.; Hwang, S.H.; Lee, S.; Suk, M.J.; Oh, S.T.; Kim, Y.D. Microstructure control of Mo-Si-B alloy for formation of continuous  $\alpha$ -Mo phase. *Int. J. Refract. Met. Hard Mater.* **2015**, *53*, 61–65. [[CrossRef](#)]
28. Li, B.; Lin, X.H.; Zhang, G.J.; Li, L.P.; Zhang, P.X. Optimization of multi-phase Mo-12Si-8.5B alloy by SiC whisker. *JOM* **2018**, *70*, 2529–2536. [[CrossRef](#)]